CHEMISTRY OF MATERIALS
Article

Chem. Mater. **2009,** *21,* 5203–5214 5203
DOI:10.1021/cm9021358

Effect of Nonmagnetic Substituents Mg and Zn on the Phase Competition in the Multiferroic Antiferromagnet $MnWO_4$

Lynda Meddar,[†] Michael Josse,[‡] Philippe Deniard,[†] Carole La,[†] Gilles André,[§] Françoise Damay,[§] Vaclav Petricek,[⊥] Stéphane Jobic,[†] Myung-Hwan Whangbo,[▽] Mario Maglione,[‡] and Christophe Payen*[,†]

[†]*Institut des Matériaux Jean Rouxel (IMN), Université de Nantes-CNRS, Nantes, France,* [‡]*CNRS, Université de Bordeaux, ICMCB, Bordeaux, France,* [§]*Laboratoire Léon Brillouin (LLB), CEA-CNRS UMR 12, 91191 Gif-sur-Yvette cedex, France,* [⊥]*Institute of Physics, Academy of Sciences of the Czech Republic, Praha, and* [▽]*Department of Chemistry, North Carolina State University, Raleigh, North Carolina 27695-8204*

Received July 14, 2009. Revised Manuscript Received September 23, 2009

The effects of substituting nonmagnetic Mg^{2+} and Zn^{2+} ions for the Mn^{2+} ($S = 5/2$) ions on the structural, magnetic, and dielectric properties of the multiferroic frustrated antiferromagnet $MnWO_4$ were investigated. Polycrystalline samples of $Mn_{1-x}Mg_xWO_4$ and $Mn_{1-x}Zn_xWO_4$ ($0 \le x \le 0.3$) solid solutions were prepared via a solid-state route and characterized via X-ray and neutron diffraction, magnetization, and dielectric permittivity measurements. Mg and Zn substitutions result in very similar effects. The Néel temperature (T_N), the AF3-to-AF2 magnetic phase-transition temperature (T_2), and the critical ferroelectric temperature ($T_c = T_2$) of $MnWO_4$ are reduced upon nonmagnetic doping. At the lowest temperature ($T = 1.5$ K), the incommensurate magnetic structure for $x(Mg) = 0.15$ and $x(Zn) = 0.15$ corresponds to either a sinusoidal spin arrangement or an elliptical spin-spiral phase similar to the polar AF2 structure observed in $MnWO_4$. These findings were discussed by considering the effects of the Mg and Zn substitutions on the crystal lattice and on the spin exchange network of $MnWO_4$.

1. Introduction

Recently, multiferroic materials, in which the ferroelectric polarization is driven by the magnetic ordering, have become a subject of much attention, because of their magnetoelectric effect.[1] Many of these single-phase materials possess geometrically frustrated spin networks, which generally prevent the formation of conventional collinear spin structures. In this class of antiferromagnetic materials, an incommensurate (ICM) magnetic structure with spiral-spin order can result, and the magnetic phase transition to this noncentrosymetrically ordered magnetic state can induce a spontaneous electric polarization via the spin-orbit coupling. The ferroelectric order is connected to the spin-spiral structure through a double vector product, $\mathbf{p} \propto \mathbf{e}_{ij} \times (\mathbf{S}_i \times \mathbf{S}_j)$ where $\mathbf{p}$ is the local polarization and $\mathbf{e}_{ij}$ the unit vector connecting the nearest neighbor spins $\mathbf{S}_i$ and $\mathbf{S}_j$.[2,3]

Among the spin-spiral multiferroics, manganese tungstate ($MnWO_4$), in which non-Jahn−Teller Mn^{2+} (d^5) ions carry $S = 5/2$ spins, is an outstanding example.[4−6] Recent work has demonstrated that the ferroelectric and spin-spiral orders coexist and are intimately coupled in this material.[4−11] $MnWO_4$ undergoes three magnetic phase transitions under zero magnetic field below a temperature of 14 K (see Figure 1).[12] With decreasing temperature, $MnWO_4$ first transforms from a paramagnetic (PM) state to a collinear spin sinusoidal state (AF3) at a Néel temperature (T_N) of ∼13.5 K, then to a tilted elliptical spiral spin state (AF2) at T_2 ∼12.3 K, and eventually to a up−up−down−down collinear spin structure (AF1) at $T_1 \approx 8.0$ K. The magnetic structures of the AF3 and AF2 states are ICM to the lattice spacing with propagation vector $\mathbf{k} = (-0.214, 0.5, 0.457)$, whereas that

*Author to whom correspondence should be addressed. E-mail: christophe.payen@cnrs-imn.fr.

(1) (a) Fiebig, M. *J. Phys. D* **2005**, *38*, R123. (b) Tokura, Y. *Science* **2006**, *312*, 1481. (c) Cheong, S.-W.; Mostvoy, M. *Nat. Mater.* **2007**, *6*, 13.
(2) Katsura, H.; Nagaosa, N.; Balatsky, V.A. *Phys. Rev. Lett.* **2005**, *95*, 057205.
(3) Sergienko, I.A.; Dagotto, E. *Phys. Rev. B* **2006**, *73*, 094434.
(4) Taniguchi, K.; Abe, N.; Takenobu, T.; Iwasa, Y.; Arima, T. *Phys. Rev. Lett.* **2006**, *97*, 097203.
(5) Arkenbout, A. H.; Palstra, T.T.M.; Siegrist, T.; Kimura, T. *Phys. Rev. B* **2006**, *74*, 184431.
(6) Heyer, O.; Hollmann, N.; Klassen, I.; Jodlauk, S.; Bohatý, L.; Becker, P.; Mydosh, J.A.; Lorenz, T.; Khomskii *J. Phys.: Condens. Matter* **2006**, *18*, L471.
(7) Taniguchi, K.; Abe, N.; Sagayama, H.; Ohtani, S.; Takenobu, T.; Iwasa, Y.; Arima, T. *Phys. Rev. B* **2008**, *77*, 64408.
(8) Sagayama, H.; Taniguchi, K.; Abe, N.; Arima, T.; Soda, M.; Matsuura, M.; Hirota, K. *Phys. Rev. B* **2008**, *77*, 220407(R).
(9) Taniguchi, K.; Abe, N.; Umetsu, H.; Aruga Katori, H.; Arima, T. *Phys. Rev. Lett.* **2008**, *101*, 207205.
(10) Meier, D.; Maringer, M.; Lottermoser, Th.; Becker, P.; Bohaty, L.; Fiebig, M. *Phys. Rev. Lett.* **2009**, *102*, 107202.
(11) Taniguchi, K.; Abe, N.; Ohtani, S.; Arima, T. *Phys. Rev. Lett.* **2009**, *102*, 147201.
(12) Lautenschläger, G.; Weitzel, H.; Vogt, T.; Hock, R.; Böhm, A.; Bonnet, M.; Fuess, H. *Phys. Rev. B* **1993**, *48*, 6087.

Published on Web 10/07/2009

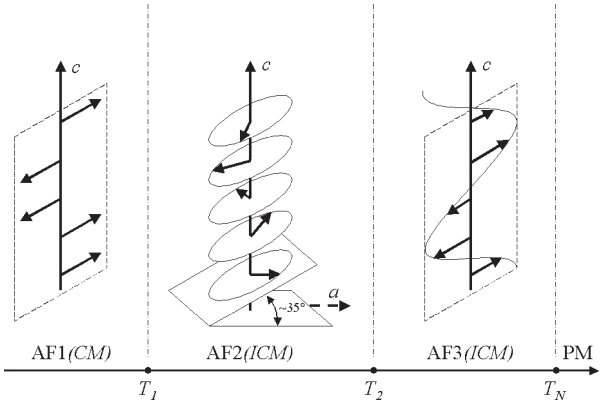

Figure 1. Schematic diagram showing the three ordered magnetic states of $MnWO_4$ below 14 K, where $T_N = 13.5$ K, $T_2 = 12.3$ K, and $T_1 = 8.0$ K. In the collinear AF1 and AF3 magnetic states, the Mn-spins are aligned with the easy axis of magnetization that lies in the *ac*-plane at an angle of 35° with the *a*-axis. In the spin-spiral AF2 phase, the Mn-spin has an additional component along the *b*-direction.

of the AF1 state is commensurate (CM) with propagation vector $\mathbf{k} = (-0.25, 0.5, 0.5)$.[12] The loss of inversion symmetry due to the helical spin ordering at T_2 makes $MnWO_4$ exhibit ferroelectric polarization in the AF2 state, and T_2 is also the ferroelectric critical temperature.[4−6] In both the AF1 and AF3 states, the Mn-spins have a collinear arrangement and $MnWO_4$ does not show electric polarization since $\mathbf{p} \propto \mathbf{e}_{ij} \times (\mathbf{S}_i \times \mathbf{S}_j) = \mathbf{0}$ in these cases. Furthermore, $MnWO_4$ has a simple wolframite crystal structure, which is described by the monoclinic $P2/c$ space group.[13,14] The building blocks of $MnWO_4$ are MnO_6 octahedra containing Mn^{2+} ions and WO_6 octahedra containing diamagnetic W^{6+} (d^0) ions. The MnO_6 octahedra share edges to form zigzag MnO_4 chains along the *c*-direction (see Figure 2a), and the WO_6 octahedra form zigzag WO_4 chains along the *c*-direction (see Figure 2b). The three-dimensional (3D) structure of $MnWO_4$ is obtained from these MnO_4 and WO_4 chains on sharing their octahedral corners (see Figure 2c). Thus, in $MnWO_4$, layers of magnetic Mn^{2+} ions parallel to the *bc*-plane alternate with layers of diamagnetic W^{6+} ions parallel to the *bc*-plane along the *a*-direction.

The existence of successive phase transitions in $MnWO_4$ has been attributed to competing magnetic interactions in the presence of weak magnetic anisotropy at each Mn^{2+} site.[12,15] Indeed, the ICM components of the propagation vector of the AF3 and AF2 states, $\mathbf{k} = (-0.214, 0.5, 0.457)$, suggest that the spin interactions are frustrated along the *a*- and *c*-directions. It is well known that sufficiently strong frustration in a magnet results in a large number of quasi-degenerate low-energy states that can compete for the ground state. With decreasing temperature from the PM state, a weak single-ion anisotropy first selects the AF3 state in which Mn-spins are actually aligned along the easy axis of magnetization (see Figure 1). However, this AF3 state is "semi-ordered", because the spin fluctuations due to the frustration are still strong enough to induce a sinusoidal modulation of the Mn-spin amplitude. On further cooling, $MnWO_4$ enters the more ordered spin-spiral AF2 arrangement to reduce the extent of spin frustration. Magnetic entropy is further reduced upon cooling by the onset of the phase transition to the AF1 state. This state has collinear spin order with no spin-amplitude reduction but is still spin-frustrated as it differs from the "up−down−up−down" Néel state. Besides, a recent density functional theory (DFT) study revealed that the ICM state AF2 is more stable than the CM state AF1, in terms of the spin exchange interactions alone,[15] and the occurrence of the AF1 state below T_1 were attributed to the presence of weak magnetic anisotropy at each Mn^{2+} site. Clearly, the phase competition in $MnWO_4$ should be modified by small perturbations such as external pressure or intentional chemical doping. A substitutional doping should tune both the spin interactions and magnetic anisotropy and, therefore, provides a way of better understanding the low-temperature properties of $MnWO_4$ and of modulating these properties. Actually, in $Mn_{1-x}Fe_xWO_4$ and $Mn_{1-x}Co_xWO_4$ solid solutions,[16,17] the substitution of magnetic Fe^{2+} ($S = 2$) or Co^{2+} ($S = 3/2$) ions for Mn^{2+}, which introduces extra Mn−M and M−M (M = Fe, Co) spin interactions, along with a different local magnetic anisotropy determined by the M^{2+} ions, modifies the phase competition. The Fe substitution stabilizes the CM AF1 order,[16] whereas the Co doping suppresses this AF1 state and stabilizes the spin-spiral AF2 magnetic structure down to 4 K.[17] On the other hand, no study of the effect of nonmagnetic substitution on the multiferroic properties of $MnWO_4$ has been reported so far.

In this paper, we report an initial study of the effect of nonmagnetic substitution at the Mn site on the structural, magnetic, and dielectric properties of $MnWO_4$. The principal goal of this work was to test the robustness of the phase transitions and of the multiferroic state AF2 against nonmagnetic dopants. Mg^{2+} and Zn^{2+} ions were chosen because pure MWO_4 (M = Mg, Zn) and $MnWO_4$ are isostructural and possess only small differences in lattice cell volume (~5 %). Therefore, a moderate doping should induce only little change in the crystal lattice of $MnWO_4$, and $MnWO_4$ should be diluted by Mg or Zn substituents without drastic changes of the magnetic interactions (e.g., due to local symmetry and bond-length variations). The use of two different dopants (Mg^{2+} and Zn^{2+}) will help identify "universal" behaviors that are essentially due to the dilution of the magnetic network.

2. Experimental Section

Powder and ceramic samples of $Mn_{1-x}Mg_xWO_4$ and $Mn_{1-x}Zn_xWO_4$ ($x = 0$, 0.05, 0.10, 0.15, 0.20, 0.25, 0.30) solid solutions were prepared using a standard solid-state reaction method, starting from high-purity MnO, WO_3, MgO, or ZnO

(13) Weitzel, H. *Z. Kristallogr., Kristallgeom., Kristallphys., Kristallchem.* **1976**, *144*, 238.
(14) Macavei, J.; Schulz, H. *Z. Kristallogr.* **1993**, *207*, 193.
(15) Tian, C.; Lee, C.; Xiang, H.; Zhang, Y.; Payen, C.; Jobic, S.; Whangbo, M.-H. *Phys. Rev. B* **2009**, *80*(10), 104426.
(16) Ye, F.; Ren, Y.; Fernandez-Baca, J. A.; Mook, H. A.; Lynn, J. W.; Chaudhury, R. P.; Wang, Y. Q.; Lorenz, B.; Chu, C. W. *Phys. Rev. B* **2009**, *78*, 193101.
(17) Song, Y.-S.; Chung, J.-H.; Park, J. M. S.; Choi, Y.-N. *Phys. Rev. B* **2009**, *79*, 224415.

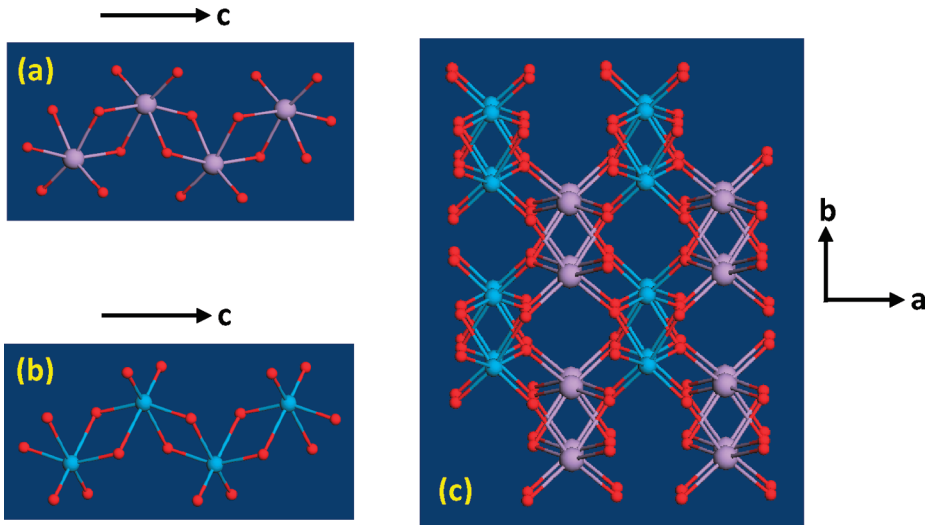

Figure 2. Perspective views of (a) a zigzag MnO_4 chain, (b) a zigzag WO_4 chain, and (c) the three-dimensional (3D) arrangement of the MnO_4 and WO_4 chains in $MnWO_4$.

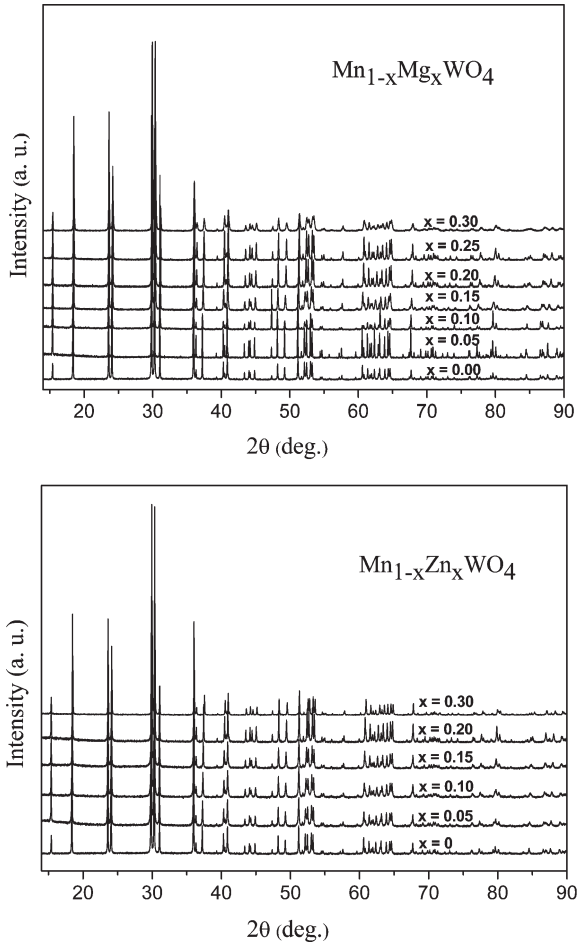

Figure 3. Room-temperature XRD patterns of $Mn_{1-x}Mg_xWO_4$ and $Mn_{1-x}Zn_xWO_4$ powder samples ($x \leq 0.3$).

commercial powders with submicrometer particle size. The crystallinity and purity of the dried starting oxides were examined by X-ray diffraction (XRD) measurements. Stoichiometric amounts of these oxides were ball-milled in ethanol for several hours, dried, and then pressed to form pellets. The pellets were heated at 850 °C for 30 h in air with an intermediate mechanical grinding. The pellets were then ground and the resultant powders were used to make dense ceramics suitable for dielectric permittivity measurements. These disk-shaped samples were sintered at temperatures in the range of 1000−1150 °C for 1 h in air. The sintering behavior of the samples was studied by measuring the change in length of a cylindrical sample with increasing temperature using a commercial dilatometer. The relative density of all sintered samples was >90%.

Chemical analyses were performed using energy-dispersive X-ray spectroscopy (EDX) at different positions on the sample surfaces. Within the experimental accuracy of a few percent, the results agree with the nominal concentrations of the metal atoms (i.e., Mn, W, Mg, or Zn). For the structural analysis, powder XRD data were collected at room temperature with a 2θ scan step of 0.0084° on a Bruker diffractometer (Model D8 Advance) that was equipped with a Vantec position-sensitive detector using Cu $K\alpha_1$ radiation (Ge monochromator, $\lambda = 1.540598$ Å). Neutron powder diffraction (NPD) patterns of 6-g samples of $Mn_{1-x}Zn_xWO_4$ and $Mn_{1-x}Mg_xWO_4$ with nominal $x = 0.15$ were taken at LLB. High-resolution diffraction data were collected at $T = 300$ K on the 3T2 diffractometer (incoming wavelength of $\lambda = 1.22537$ Å). The magnetic structures were examined using the G4.1 instrument (incoming wavelength of $\lambda = 2.4226$ Å). XRD and NPD patterns were analyzed using JANA 2006 and FULLPROF programs.[18,19]

A SQUID magnetometer (MPMS Quantum Design) was used to investigate the magnetic properties of the specimens. The temperature dependence of the zero-field-cooled (ZFC) and field-cooled (FC) dc magnetization was measured down to 2 K. In the FC mode, the applied field is switched on in the paramagnetic regime, and the measurements are made while cooling across the transition temperatures to 2 K. The ZFC heating and FC cooling rates were ±0.03 K/min. The susceptibility (χ) was defined as the ratio of the dc magnetization M to the applied field H (i.e., $\chi = M/H$).

Dielectric measurements were performed at ICMCB on sintered disks using a Hewlett−Packard Model HP4194a impedance bridge. Samples were placed in a Quantum Design Physical Properties Measurement System (PPMS). Prior to these measurements, after deposing gold electrodes on the circular faces of

(18) Petricek, V.; Dusek, M.; Palatinus, L. *The Crystallographic Computing System JANA*, 2006 Beta; Academy of Sciences: Praha, Czech Republic, 2006.
(19) Rodriguez-Carvajal, J. *Physica B* **1993**, *192*, 55.

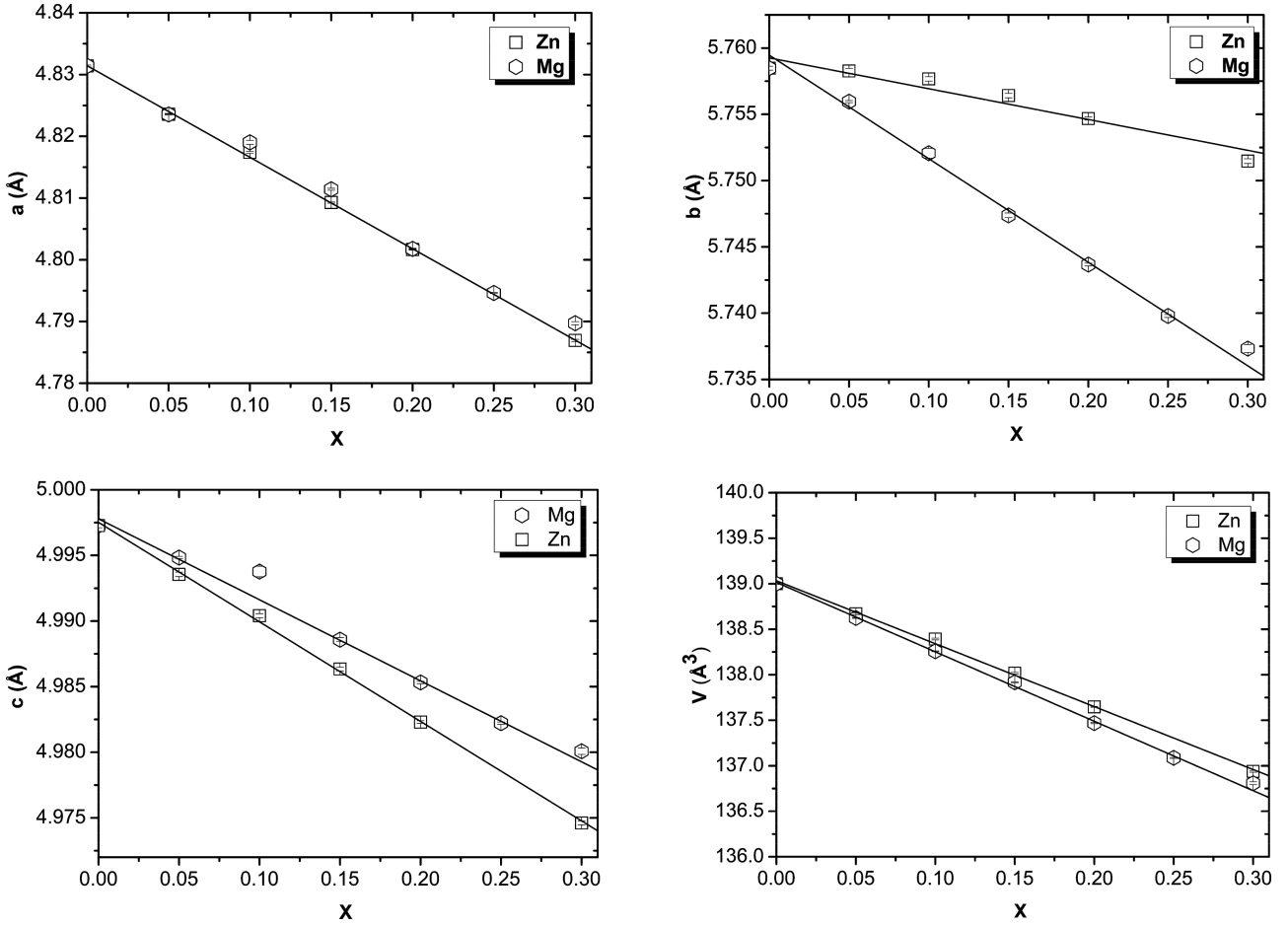

Figure 4. Refined lattice parameters and cell volumes of $Mn_{1-x}M_xWO_4$ (M = Mg, Zn) powder samples ($x \leq 0.3$) as a function of x. The solid lines are drawn through the lattice parameter points as a guide for the eyes. The solid lines drawn in the cell-volume plots refer to the relationship, $V(x) = (1 - x)V(MnWO_4) + xV(MWO_4)$, for M = Mg and Zn. The cell volumes of the pure MWO_4 (M = Mg, Zn) phases were taken from the literature.[22]

the disks by cathodic sputtering, silver wires were attached to the top and bottom of the pellets, using a silver paste. These measurements were conducted in the frequency range of 10^2-10^3 kHz and in the temperature range of 4−16 K. All the capacitances and loss factor (tan δ) data were collected at heating and cooling rates of 0.2 K/min and at zero magnetic field. All samples displayed very small capacitances (~7 pF), and the ferroelectric transition was associated with even smaller variations of the capacitance (typically a few fF).

3. Results

3.1. Room-Temperature X-ray and Neutron Diffraction. Figure 3 presents the room-temperature XRD patterns of the $Mn_{1-x}Mg_xWO_4$ and $Mn_{1-x}Zn_xWO_4$ powder samples ($x \leq 0.3$). All patterns show very narrow diffraction peaks without any splitting or extra reflection and are consistent with those reported for the monoclinic $P2/c$ Wolframite structure of $MnWO_4$ (JCPDS File Card No. 13-0434). Rietveld refinements of these patterns were performed on the basis of the literature $P2/c$ structural model of $MnWO_4$, using a random distribution of the Mn and Mg or Zn ions on the Wyckoff 2f position. All positions were fully occupied. Because of the presence of the heavy W^{6+} ion and the small difference in the numbers of electrons between Mn^{2+} and Zn^{2+} ions, the fractional occupancies for Mg or Zn at the 2f Mn site were held fixed to the nominal Mg or Zn molar content (x). With this model, all patterns could be successfully refined. The M−O (M = Mn, Mg, Zn) and W−O bond lengths calculated from the refined lattice parameters and atomic coordinates are in good agreement with those observed for Wolframite MWO_4 (M = Mn, Mg, Zn). Furthermore, the corresponding bond valence sum calculations[20] are consistent with the presence of M^{2+} (M = Mn, Mg, Zn), W^{6+}, and O^{2-} ions.

Figure 4 shows the refined lattice parameters and the calculated cell volume of $Mn_{1-x}M_xWO_4$ (M = Zn or Mg) as a function of the nominal molar concentration x. As expected from Vegard's law, the lattice parameters (a, b, and c) decrease as x increases, because Mg^{2+} or Zn^{2+} ions are smaller in size than Mn^{2+}; the ionic radii of Mg^{2+} and Zn^{2+} ions at an octahedral site are 0.72 and 0.74 Å, respectively, whereas that of a high-spin Mn^{2+} ion at an octahedral site is 0.83 Å.[21] Furthermore, the cell volume of $Mn_{1-x}M_xWO_4$ (M = Zn or Mg) evolves linearly as the weighted average between those of $MnWO_4$ and MWO_4 (M = Zn or Mg), $V(x) = (1 - x)V(MnWO_4) + xV(MWO_4)$, suggesting that the actual concentration of M

(20) Brown, I. D.; Altermatt, D. *Acta Crystallogr., Sect. B: Struct. Sci.* **1985**, *B41*, 244.
(21) Shannon, R. D. *Acta Crystallogr., Sect. A: Crst. Phys., Diffr., Theor. Gen. Crystallogr.* **1976**, *A32*, 751.

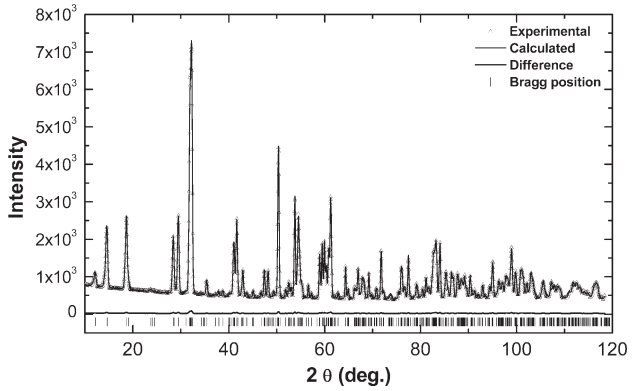

Figure 5. Observed (triangles) and calculated (solid curve) neutron powder diffraction (NPD) patterns of $Mn_{0.85}Zn_{0.15}WO_4$ collected on 3T2 of the LLB at 300 K using neutrons of $\lambda = 1.2254$ Å. The tickmarks indicate the positions of the nuclear Bragg reflections. The lower curve shows the difference between the observed and calculated data on the same scale.

in $Mn_{1-x}M_xWO_4$ (M = Zn or Mg) is equal to, or very close to, the nominal value x.

Because the Mg or Zn content could not be determined from the refinements of the XRD patterns, NPD data of a sample of $Mn_{1-x}Zn_xWO_4$ with nominal value of $x = 0.15$ were collected at room temperature (see Figure 5). Rietveld refinements were conducted based on the results obtained from the XRD measurements using the coherent nuclear scattering lengths $b(\mathrm{Mn}) = -3.73$ fm, $b(\mathrm{Zn}) = 5.68$ fm, $b(\mathrm{W}) = 4.86$ fm, and $b(\mathrm{O}) = 5.803$ fm. The precision in the determination of the Mn/Zn occupation at the 2f site clearly should be satisfactory, because of the contrast in scattering lengths between Mn and Zn. With the occupancies of the W and O sites kept fixed, the Rietveld agreements factors were $R_p = 1.84$, $R_{wp} = 2.38$, goodness of fit (GOF) = 0.67. The refined lattice parameters, atomic positions, bond distances, and bond valence sums are similar to those obtained from XRD refinement. The refined Zn occupancy at the 2f site, 0.149(4), is in excellent agreement with the nominal value $x = 0.15$. Attempts to refine the NPD pattern with W atoms at the Mn 2f site and with Zn or Mn atoms at the W atom sites yielded worse results. Hereafter, therefore, we will consider that the actual Mg or Zn concentrations are equal to their nominal values x.

3.2. Bulk Magnetic Properties. We first examine the bulk magnetic properties at temperatures above the magnetic phase-transition temperatures of $MnWO_4$ ($T_N = 13.5$ K). Figure 6 shows the reciprocal susceptibility data of powder samples of $Mn_{1-x}Mg_xWO_4$ and $Mn_{1-x}Zn_xWO_4$ ($x \le 0.3$). Above $T \approx 20$ K, all samples exhibit Curie−Weiss behavior, $1/\chi(x,T) = [T - \theta(x)]/C(x)$. The molar Curie constants ($C(x)$) and the absolute Weiss temperatures ($|\theta(x)|$) obtained from Curie−Weiss fits to the high-temperature susceptibility data ($T > 150$ K) are plotted as a function of x in Figure 7. The results for $MnWO_4$—namely, $C(0) \approx 4.25$ cm^3 K/mol and

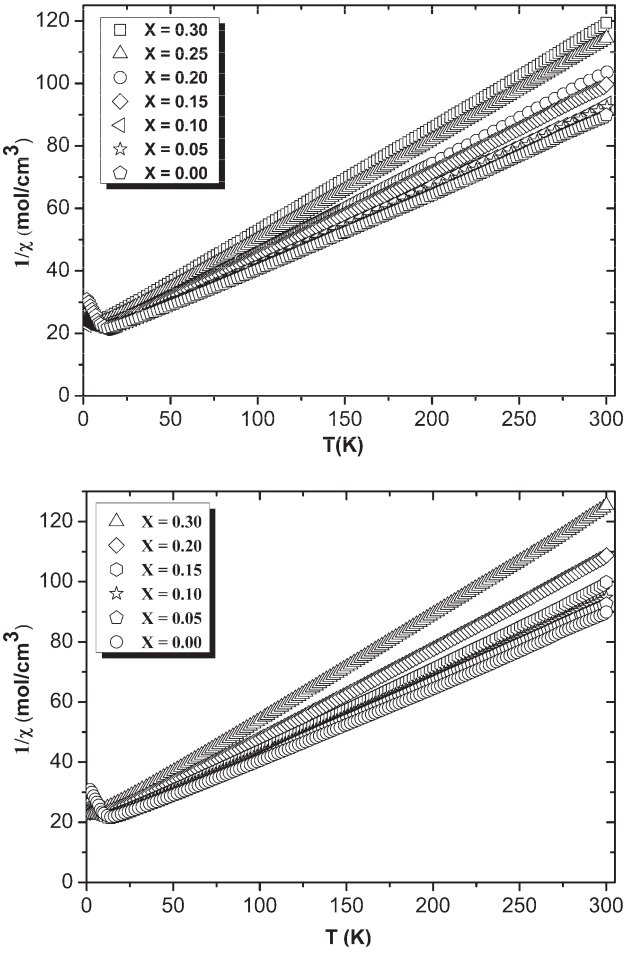

Figure 6. Temperature dependence of the reciprocal ZFC magnetic susceptibility $1/\chi(x,T)$ determined for the powder samples of $Mn_{1-x}Mg_xWO_4$ (top) and $Mn_{1-x}Zn_xWO_4$ (bottom) ($x \le 0.3$) obtained at $\mu_0 H = 0.1$ T.

$\theta(0) \approx -71$ K—compare well with those reported in the literature.[4,23] For both nonmagnetic dopants, the molar Curie constant $C(x)$ and the absolute Weiss temperature $|\theta(x)|$ decrease linearly as x increases, as $C(x) = (1 - x)C(0)$ and $|\theta(x)| = (1 - x)|\theta(0)|$, respectively (see Figure 7). These linear behaviors are expected in the high-temperature limit for any randomly diluted antiferromagnet.[24] As a matter of fact, the Curie−Weiss fits could be done above $T \approx 2|\theta(x)|$, where the Curie−Weiss law is strictly applicable. In this mean-field regime, the Weiss temperature is given by the well-known relationship $\theta = \frac{S(S+1)}{3k_B}\sum_i z_i J_i$ where J_i is the exchange coupling between a central spin and the z_i spins linked by J_i. Within this approach, the dilution-induced decrease in $|\theta(x)|$ can be explained solely in terms of the increase in the missing magnetic bonds caused by the nonmagnetic substitution. The observed Weiss temperatures are negative, showing that the principal magnetic interactions remain antiferromagnetic in the diluted systems. The effective moments per Mn^{2+}, calculated from the Curie constant $C(x)$, are in the range of 5.75−5.9 μ_B, which is consistent with the spin only value of 5.92 μ_B.

(22) Sleight, A. W. *Acta Crystallogr., Sect. B: Struct. Crystallogr. Cryst. Chem.* **1972**, *B28*, 2899.
(23) Dachs, H. *Solid State Commun.* **1969**, *7*, 1015.
(24) Spalek, J.; Lewicki, A.; Tarnawski, Z.; Furdyna, J. K.; Galazka, R. R.; Obuszko, Z. *Phys. Rev. B* **1986**, *33*, 3407.

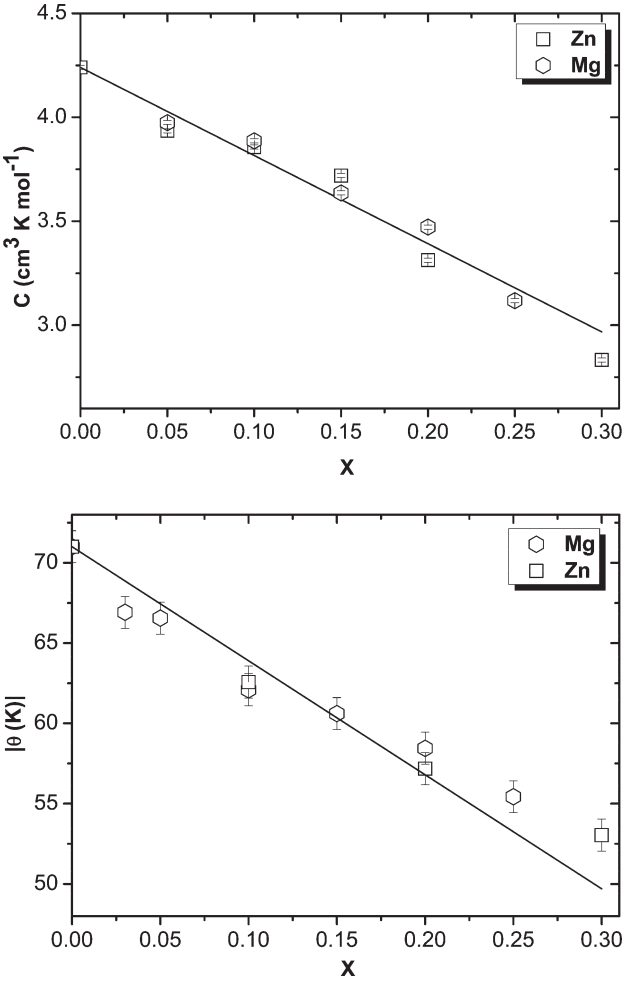

Figure 7. Molar Curie constants $C(x)$ (top) and absolute Weiss temperatures $|\theta(x)|$ (bottom) of $Mn_{1-x}M_xWO_4$ (M = Mg, Zn) as a function of x. The solid line refers to the relationship $C(x) = (1 - x) \times C(0)$ for the Curie constants, and $|\theta(x)| = (1 - x) \times |\theta(0)|$ for the Weiss temperatures.

We now analyze the low-temperature magnetic susceptibility data of $Mn_{1-x}Mg_xWO_4$ and $Mn_{1-x}Zn_xWO_4$ powder samples ($0 \le x \le 0.3$), shown in Figures 8 and 9. The data for the $MnWO_4$ ($x = 0$) powder sample are consistent with those obtained for single-crystal samples,[4,5] showing three magnetic phase transitions at $T_1 \approx 7.5$ K, $T_2 \approx 12.5$ K, $T_N \approx 13.5$ K, which we estimated from the peak positions in the derivative $d\chi/dT$ curve obtained from the ZFC heating curve (Figure 8). A small but significant thermal hysteresis around T_1 is evidenced by comparing the ZFC heating and the FC cooling curves (see Figure 8). This feature is fully consistent with the first-order nature of the AF1-to-AF2 phase transition in $MnWO_4$. For the substituted compounds, no difference between the ZFC heating and FC cooling traces was observed down to 2 K, for all x values, up to the highest value of 0.30. As shown in Figure 9, the substituted samples do not show any anomaly in the susceptibility that can correspond to the AF1-to-AF2 phase transition observed for $MnWO_4$. This is also clearly seen in the derivative $d\chi/dT$ curves shown in Figure 10. For both nonmagnetic ions Zn^{2+} and Mg^{2+}, both the AF2-to-AF3 transition temperature T_2 and the Néel temperature T_N

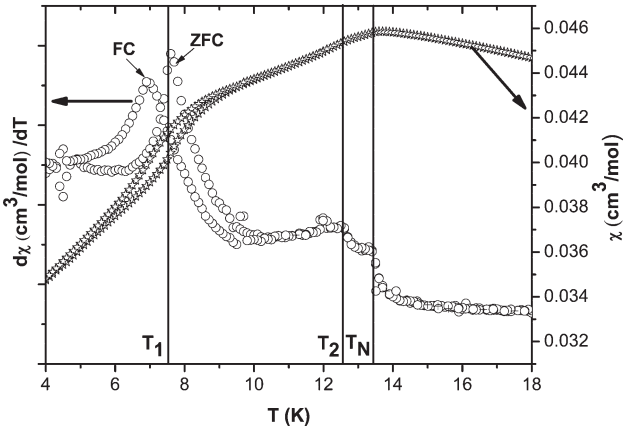

Figure 8. Temperature dependence of the ZFC and FC magnetic susceptibility of a powder sample of $MnWO_4$ obtained at $\mu_0 H = 0.1$ T (star symbols, ☆). Open circles (○) show the corresponding derivative $d\chi/dT$ curves. Vertical lines indicate the magnetic phase-transition temperatures, as determined from the peaks in the ZFC derivative.

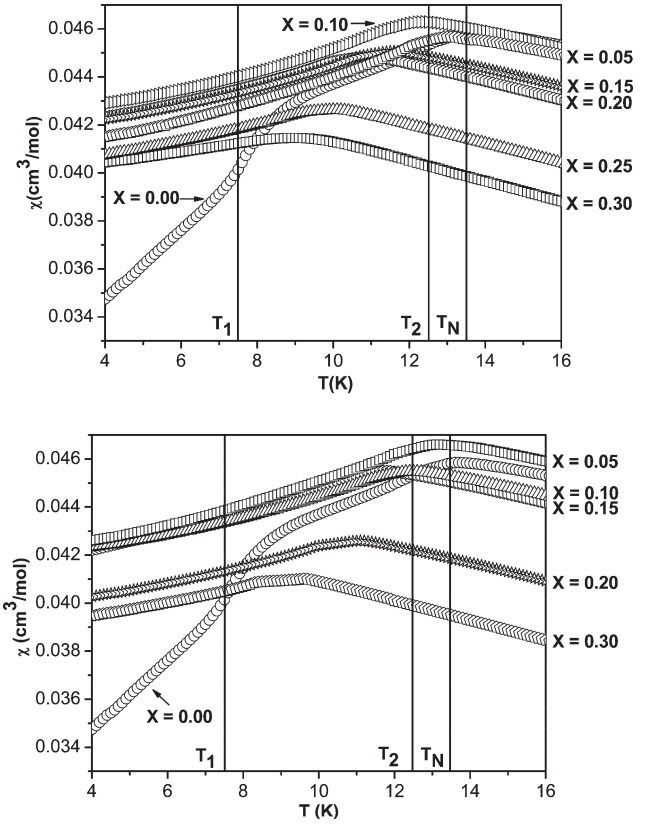

Figure 9. Temperature dependence of the ZFC molar magnetic susceptibility of $Mn_{1-x}Mg_xWO_4$ (top) and $Mn_{1-x}Zn_xWO_4$ (bottom) powder samples ($x \le 0.3$) obtained at $\mu_0 H = 0.1$ T. Vertical lines indicate the magnetic phase-transition temperatures for $MnWO_4$.

decrease as x increases, both at a rate of approximately −0.13 K per mol % of Mg or Zn. The values of T_2 and T_N are plotted as a function of x in Figure 11. Except for x(Mg) = 0.30, the peak anomalies for T_2 and T_N are well-defined, hence, leading to accurate determinations of these transition temperatures. This also indicates that the prepared samples are homogeneous. Overall, the magnetic properties of the substituted compounds are independent of the nature of the nonmagnetic dopant.

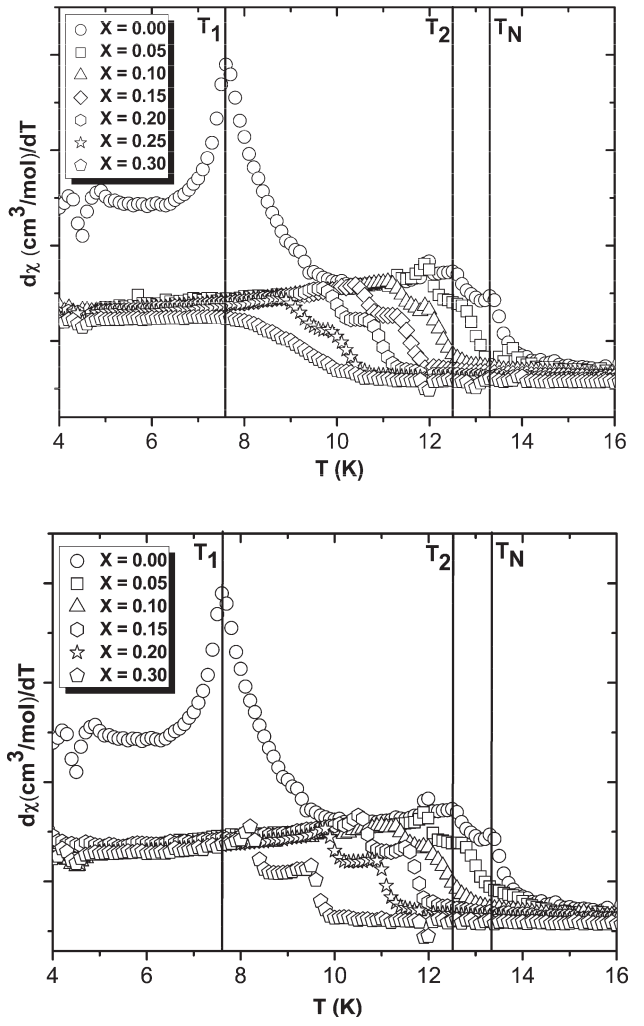

Figure 10. Derivative of the temperature-dependent ZFC magnetic susceptibility of $Mn_{1-x}Mg_xWO_4$ (top) and $Mn_{1-x}Zn_xWO_4$ (bottom) powder samples ($x \leq 0.3$). Vertical lines indicate the magnetic phase-transition temperatures of $MnWO_4$.

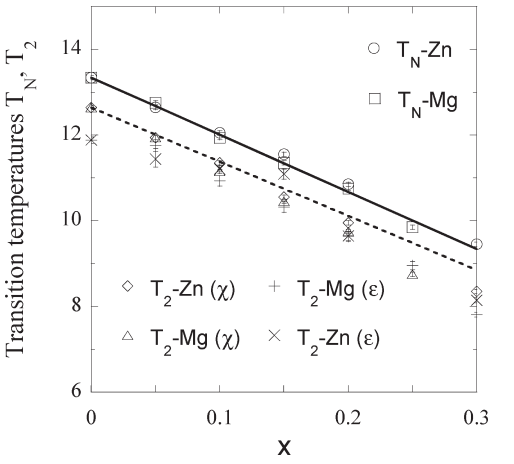

Figure 11. AF2-to-AF3 and Néel transition temperatures (T_2 and T_N, respectively), plotted as a function of Mg or Zn concentration (x). $T_2(\chi)$ and $T_2(\varepsilon)$ are the values determined from the magnetic susceptibility and dielectric measurements, respectively. The prediction of mean-field theory for T_N and $T_2(\chi)$ reductions of randomly diluted magnets are given by the solid and dashed lines, respectively. For the description of $T_2(\varepsilon)$, see section 3.3.

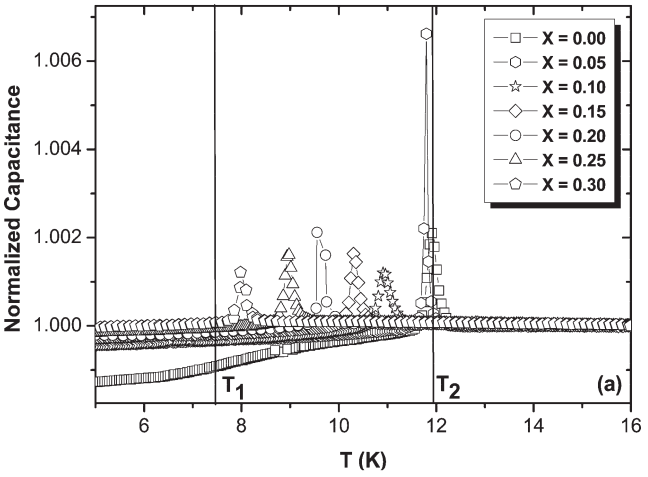

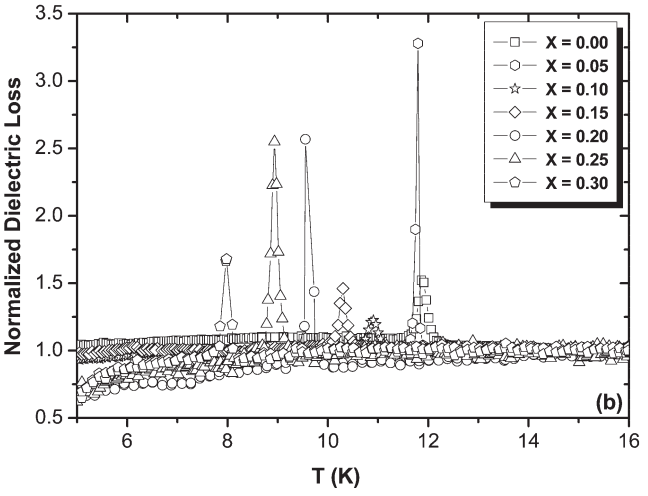

Figure 12. Temperature dependence of the capacitance and the loss factor of $Mn_{1-x}Mg_xWO_4$ ceramic samples ($x \leq 0.3$), measured at 788 kHz during the heating run. The capacitance and loss tangent data were arbitrarily normalized to the values measured at 16 K.

3.3. Dielectric Properties at Zero Magnetic Field. To gain insight into ferroelectric transitions and possible dielectric dispersions at low temperature, the dielectric responses of dense ceramic samples of $Mn_{1-x}M_xWO_4$ (M = Mg, Zn) were investigated between 100 kHz and 1 MHz at temperatures from 4 K to 16 K and at zero magnetic field. No dielectric dispersion was observed in these samples, regardless of the experimental conditions. This lack of dispersion is proof of the ferroelectric nature of the observed dielectric anomalies. For a given frequency, tiny differences between the heating and cooling data were observed. These differences corresponded to a thermal hysteresis of ~0.05 K and were due to the value of the heating and cooling rate of 0.2 K/min rather than a physical hysteresis. The temperature-dependent capacitance and loss tangent of the $Mn_{1-x}Mg_xWO_4$ and $Mn_{1-x}Zn_xWO_4$ ceramics ($x \leq 0.3$) are shown in Figures 12 and 13, respectively. For $MnWO_4$, a sharp peak is observed in both the capacitance and loss tangent at $T_2 \approx$ 12 K, which is consistent with the results obtained on single crystals.[5] With decreasing temperature, there is a decrease in the capacitance that corresponds to the stepwise transition previously seen at $T_1 \approx 7.5$ K on single crystals, regardless of the crystal orientation.[5] This transition is

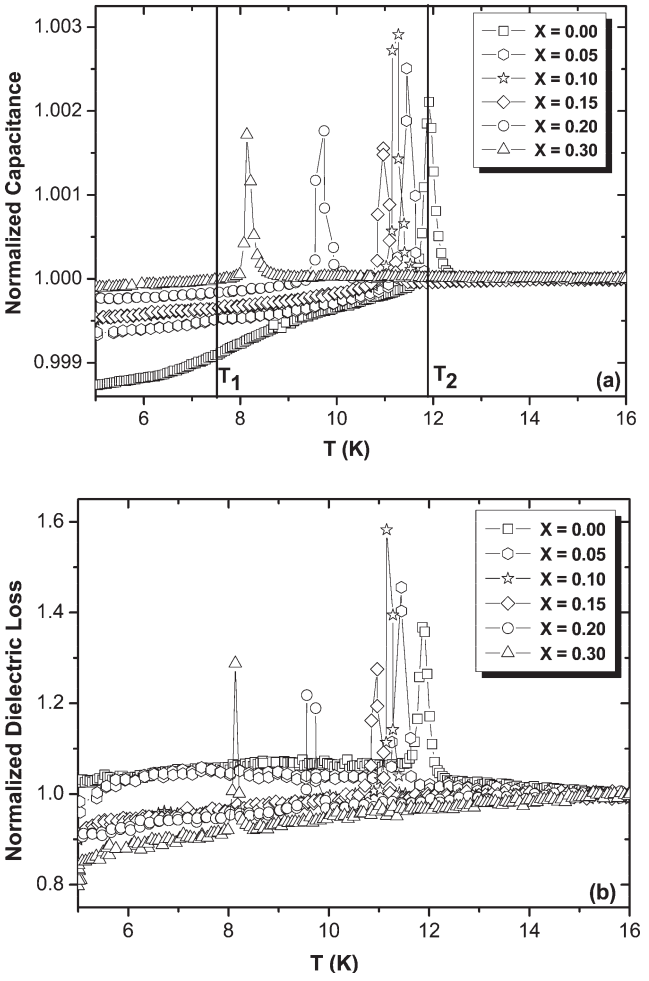

Figure 13. Temperature dependence of the capacitance and the loss factor of $Mn_{1-x}Zn_xWO_4$ ceramic samples ($x \leq 0.3$), measured at 788 kHz during the heating run. The capacitance and loss tangent data were arbitrarily normalized to the values measured at 16 K.

due to the disappearance of the ferroelectric polarization when cooling across the AF2-to-AF1 transition. Here, the broadening of this anomaly can be related to the polycrystalline state. Nevertheless, a small step in the loss factor is observed at $T_1 \approx 7.9$ K (see Figure 14).

For all the substituted samples, the sharp peak associated with the AF3-to-AF2 transition preserves its shape upon doping. The peak position in the capacitance is the same as that in the dissipation factor, and both peaks shift gradually to lower temperature with increasing substitution. The widths of the peaks do not change significantly with x (except for the case of $x = 0.05$, which is reproducible but unaccounted for). The peak positions are independent of frequency. Thus, these maxima in the capacitance and loss tangent correspond to the ferroelectric transition temperatures $T_2(\varepsilon)$. As shown in Figure 11, the x-dependence of $T_2(\varepsilon)$, as determined from the dielectric properties, is practically the same as that of $T_2(\chi)$, which is determined from magnetic susceptibilities. In the Mg-substituted samples with $x \leq 0.15$, an additional low-temperature anomaly is detected below $T_2(\varepsilon)$, either as a small peak in capacitance (x(Mg) = 0.10 and 0.15) or a weak stepwise anomaly in loss factor (x(Mg) = 0.05), at

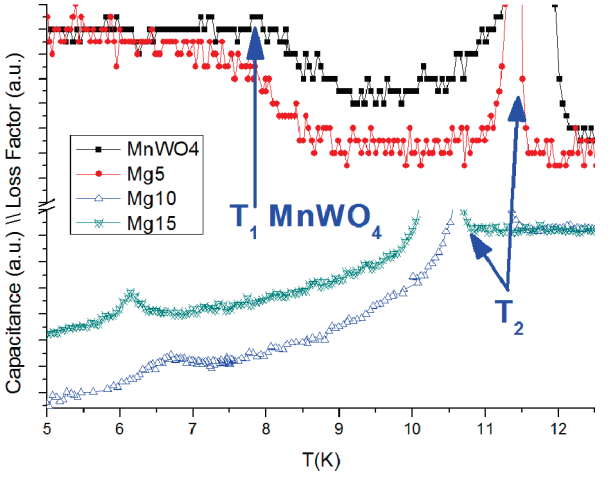

Figure 14. Low-temperature anomaly in the capacitance or loss factor for $Mn_{1-x}Mg_xWO_4$ ($x = 0.05$, 0.10, 0.15) ceramic samples.

$T_{Mg}(\varepsilon) \approx 7.6$, 6.7, and 6.1 K for x(Mg) = 0.05, 0.10, and 0.15, respectively (see Figure 14). It is tempting to attribute this anomaly to the AF2-to-AF1 transition observed at $T_1 \approx 7.9$ K in $MnWO_4$. No corresponding anomaly in the magnetic response has been observed from bulk magnetization measurements and neutron diffraction (see section 3.4), but considering the small amplitude of the capacitance peak in the x(Mg) = 0.10 and x(Mg) = 0.15 samples (below 1fF), these techniques may not be sensitive enough to detect it, if there is one. For the zinc-doped samples, no similar peak or stepwise anomaly is observed, either in the capacitance or in the loss factor.

3.4. Low-Temperature Neutron Powder Diffraction. Figure 15 shows the thermal evolution of the NPD pattern of $Mn_{0.85}Zn_{0.15}WO_4$ in the temperature range of 1.5−15 K. These data were taken using the sample that was previously examined via high-resolution neutron diffraction at room temperature (see section 3.1). The relative intensities of the magnetic peaks in the NPD patterns collected for $Mn_{0.85}Mg_{0.15}WO_4$ in the same temperature range of 1.5−15 K are identical to those observed for $Mn_{0.85}Zn_{0.15}WO_4$. For both substituted samples, the AF1 phase does not show up in the NPD above 1.5 K. Above the macroscopic Néel temperature ($T_N(x = 0.15) \approx 12$ K), the patterns show only the peaks expected from the room-temperature crystal structure. In addition, a diffuse scattering with a form similar to that observed in $MnWO_4$[12] is present over a notable 2θ range centered at ~18°. This 2θ value corresponds to an elastic wave vector $Q_{el} \approx 0.8$ Å^{-1}, which is roughly the same as in $MnWO_4$. As in $MnWO_4$, this diffuse scattering disappears on cooling below ~10 K. Therefore, the diffuse scattering indicates the presence of short-range antiferromagnetic correlations that develop above the Néel temperature and disappear only below T_2 in $MnWO_4$ or T_2 ($x = 0.15$) ≈ 10.6 K in $Mn_{0.85}M_{0.15}WO_4$ (M = Mg, Zn). This disappearance corresponds to the onset of long range spin−spin correlations that do not exist even in the semi-ordered sinusoidal AF3 state. Between $T_N(x = 0.15)$ and $T_2(x = 0.15) \approx 10.6$ K, the NPD patterns contain several new magnetic Bragg peaks, which is

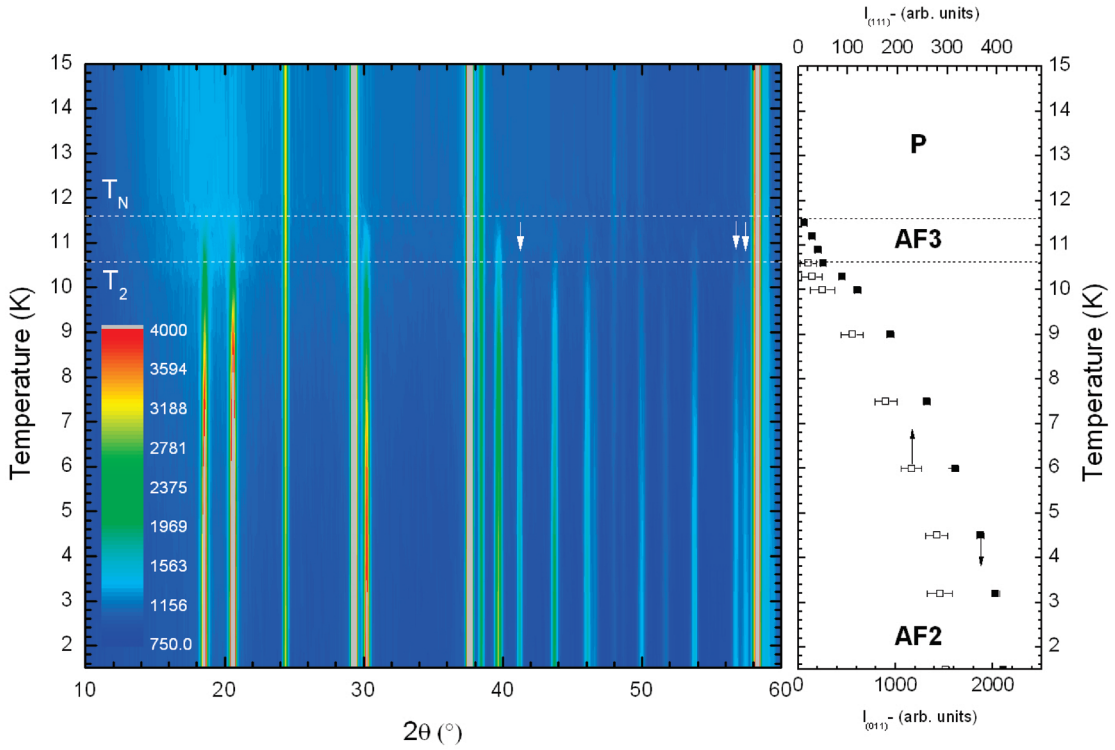

Figure 15. Temperature evolution of the G4.1 neutron diffraction patterns (left panel) and of the corresponding integrated intensity of magnetic Bragg peaks $(010)^-$ and $(111)^-$ (right panel) for $Mn_{0.85}Zn_{0.15}WO_4$. The $(hkl)^-$ indexation stands for $(hkl)-\mathbf{k}$, with $k \approx (-0.209, 0.5, 0.453)$. The arrows in the left panel indicate the extra magnetic reflections that appear below the AF3-to-AF2 phase transition temperature, $T_2(x = 0.15) \approx 10.6$ K.

Table 1. Irreducible Representations of the Propagation Vector k = (−0.209(2), 0.5, 0.453(1)) in *P*2/*c*.

	1	*c* *x*, 0, *z*
Γ_1[a]	1	a[b]
Γ_2[a]	1	$-a$[b]

[a] The magnetic representation Γ_m contains three times each representation: $\Gamma_m = 3\Gamma_1 \oplus 3\Gamma_2$. [b] The value of parameter a is defined as $a = \exp(-i\pi k_z)$.

Table 2. Basis Functions for Axial Vectors Associated with Irreducible Representations Γ_1 and Γ_2 for Wyckoff 2f Site

Γ_1	(*x*, *y*, *z*) Mn_1	(*x*, −*y*, *z*+1/2) Mn_2	Γ_2	(*x*, *y*, *z*) Mn_1	(*x*, −*y*, *z*+1/2) Mn_2
ψ_1	(1 0 0)	(*a** 0 0)	ψ_1'	(1 0 0)	(−*a** 0 0)
ψ_2	(0 1 0)	(0 −*a** 0)	ψ_2'	(0 1 0)	(0 *a** 0)
ψ_3	(0 0 1)	(0 0 *a**)	ψ_3'	(0 0 1)	(0 0 −*a**)

consistent with the ICM AF3 magnetic structure with $\mathbf{k} = (-0.214, 0.5, 0.457)$ observed for $MnWO_4$ between T_N and T_2 (see Figure 15).[12]

As shown in Figure 15, additional magnetic peaks develop below $T_2(x = 0.15) \approx 10.6$ K, in agreement with the bulk magnetic measurements. The patterns collected below this temperature are very similar to those previously obtained for $MnWO_4$ in the AF2 phase between T_2 and T_1.[12] Below $T_2(x = 0.15)$, magnetic peaks can be indexed with a new propagation vector $\mathbf{k} = (-0.209(2), 0.5, 0.453(1))$, comparable to the propagation vector $\mathbf{k} = (-0.214, 0.5, 0.457)$ obtained in the case of $MnWO_4$.[12] The corresponding ICM magnetic structure at 1.5 K has been determined by Rietveld refinement, using symmetry-adapted modes derived from representation analysis performed with the BasIreps program.[19] Table 1 lists the characters of the two one-dimensional irreducible representations of the little group G_k. The magnetic representation Γ_m calculated for the Wyckoff 2f position of the Mn atom in the *P*2/*c* space group contains three times each representation, so that there are three basis functions for each representation. Table 2 lists the corresponding basis vectors. As was already noted by Lautenschlager et al.[12] in the case of $MnWO_4$, irreducible representation Γ_2 (which describes the magnetic structure AF3 existing for $T_2 < T < T_N$ in $MnWO_4$ and $Mn_{0.85}M_{0.15}WO_4$, M = Zn, Mg) fails to provide a good agreement with the experimental data. To obtain a satisfying result, it is necessary to use a linear combination of the two irreducible representations Γ_1 and Γ_2. There are, accordingly, two indistinguishable moment configurations, with identical structure factors, that give a very good agreement factor $R_{mag} = 3.37\%$ with the data (see Figure 16). Both correspond to a coupling of the *x*- and *z*-magnetic components following Γ_2, and of the *y*-components following Γ_1. The first model is obtained by mixing ψ_1, ψ_3, and ψ_2' with real components and, therefore, corresponds to a sinusoidal structure. The second model, which is assumed to be the correct one, according to the magnetic properties and dielectric properties of $Mn_{0.85}M_{0.15}WO_4$ (M = Zn, Mg), is obtained by mixing ψ_1 and ψ_3 with real components and ψ_2' with an imaginary component. This describes an ICM spiral structure with an elliptical modulation, in which the spin rotation envelope is perpendicular to the *ac* plane, with the moments canted with regard to the *a*-axis by ~34°. The elliptical

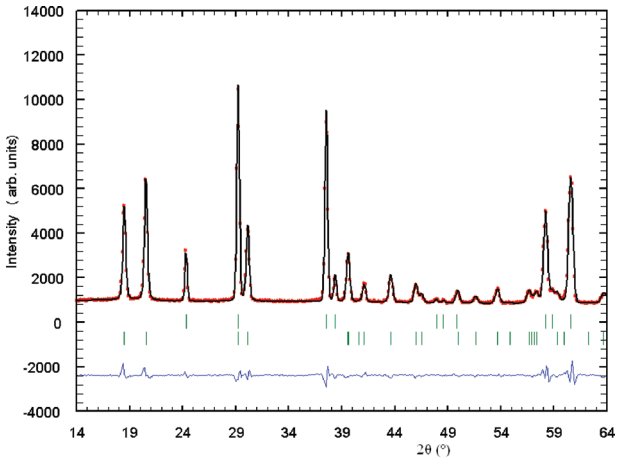

Figure 16. Rietveld refinement of the neutron diffraction data of $Mn_{0.85}Mg_{0.15}WO_4$ at 1.5 K. Open circles denote experimental data, the continuous line represents the calculated profile, and the vertical marks denote the allowed crystal and magnetic Bragg reflections. The difference between the experimental and calculated profiles is displayed at the bottom of the graph.

parameter p is 0.87. The ordered component maximum is close to 4.9 μ_B. These results are similar to those observed of $MnWO_4$.[12] In the ICM AF2 and AF3 phases of $MnWO_4$, the magnetic moment $\mathbf{m}_i$ on the ith site (i = 1 or 2) at $\mathbf{R}_i$ is described as $m_i = m_{easy} \cos(2\pi k R_i) + m_b \sin(2\pi k R_i)$, where m_{easy} and m_b are the components parallel to the magnetic easy axis and the crystallographic b-axis, respectively. The easy axis lies in the ac plane, forming an angle of $\alpha = 34°$ with the a-axis. Both the m_b component and the ellipticity $p = m_b/m_{easy}$ are zero in the sinusoidal AF3 phase, whereas m_b and p have nonzero values in the spiral AF2 phase. The refined magnetic moment and ellipticity have been reported to be $|\mathbf{m}| \approx 4.5\ \mu_B$ and $p \approx 0.8$ at 9 K, respectively.[12]

Overall, this NPD study shows that the commensurate AF1 magnetic structure of $MnWO_4$ is suppressed by the substitution in $Mn_{0.85}M_{0.15}WO_4$ (M = Zn, Mg) at T = 1.5 K. A spin-spiral phase similar to that observed in the AF2 state of $MnWO_4$ is probably stabilized by the nonmagnetic doping below $T_2(x = 0.15) \approx 10.6$ K.

4. Discussion

Our results described in the previous section show that, in essence, the properties of $Mn_{1-x}M_xWO_4$ (M = Mg, Zn) are independent of the nature of the nonmagnetic ions Mg^{2+} and Zn^{2+}. To explain this finding, we first consider the effects of the Mg and Zn substitutions on the crystal lattice, putting aside the effects on the spin−lattice. As the substitution contracts the crystal lattice of $MnWO_4$, a low doping could be equivalent to applying an external pressure. According to a recent experimental study on the pressure effect in $MnWO_4$,[25] the "chemical pressure" associated with the substitution would stabilize the nonpolar AF1 phase. Although only a slight local structural distortion is expected from the small difference in ionic radii between Mn^{2+} and M^{2+} (M = Mg, Zn), the presence of M^{2+} dopants at the Mn^{2+} sites will introduce chemical disorder. The latter could affect the phase transitions in $MnWO_4$, because a substantial spin−lattice interaction is necessary to explain the ferroelectricity associated with the AF2 spiral magnetic order. The existence of such a spin−lattice coupling has been experimentally proven by a recent synchrotron XRD study,[7] which revealed lattice modulations in the ferroelectric AF2 and paraelectric AF3 phases; the lattice propagation vector of each phase is twice the magnetic propagation vector. Furthermore, high-resolution thermal expansion measurements[25] showed clear anomalies of all three lattice parameters at T_N and T_1, and they showed a discontinuous volume change across T_1, where a locking of the magnetic modulation with the lattice occurs. Indeed, the first-order AF1-to-AF2 transition at T_1 in $MnWO_4$ is more than a mere magnetic transition. In real solids, inevitable imperfections invariably smear first-order phase transitions over certain temperature or pressure intervals. When the doping level is intentionally increased, the first-order phase transition can even be suppressed. As a matter of fact, it was observed that the impurities in flux-grown $MnWO_4$ crystals reduce the AF2-to-AF1 transition temperature T_1 but they do not modify the Néel (T_N) and AF3-to-AF2 (T_2) phase-transition temperatures.[5]

We now turn to the effects of Mg/Zn doping on the magnetic properties. In essence, the doping of nonmagnetic ions at the Mn^{2+} sites decreases not only the number of spin-exchange interactions along the zigzag MnO_4 chains along the c-direction, but also that between these chains along the a- and b-directions (see below). Nevertheless, the doped compounds remain almost as spin-frustrated as the undoped one, because the frustration parameter $|\theta|/T_N$ varies only slightly (i.e., $|\theta(x)|/T_N \approx 6$ for $x = 0$, and $|\theta(x)|/T_N \approx 5$ for $x = 0.3$). All doped samples exhibit a paramagnetic susceptibility behavior consistent with geometric spin frustration, because the mean-field Curie−Weiss regime extends to temperatures significantly lower than what could be expected from the absolute Weiss temperature. If both the undoped and doped compounds were not spin-frustrated, T_N would be of the same order of magnitude as $|\theta|$ for a three-dimensional magnetic system, or the susceptibility curve would exhibit a broad maximum in the paramagnetic regime for low-dimensional magnetic systems.

The linear reduction of T_N and T_2 shown in Figure 11 is well-explained by the prediction of mean-field theory for randomly diluted magnets, $T_c(x) = (1 - x) \times T_c(0)$, which predicts that the long-range ordering temperature decreases linearly as the amount of nonmagnetic dopants increases until all magnetic ions disappear. For nonfrustrated systems, a reduction that is faster than that predicted by the mean-field theory is expected for dopant concentrations lower than the percolation threshold.[26] Therefore, the magnetic dilution explains the reduction of the ferroelectric

(25) Chaudhury, R. P.; Yen, F.; dela Cruz, C. R.; Lorenz, B.; Wang, Y. Q.; Sun, Y. Y.; Chu, C. W. *Physica B* **2008**, *403*, 1428.

(26) Cheong, S.-W.; Cooper, A. S.; Rupp, L.W.; Batlogg, B.; Thompson, J. D.; Fisk, Z. *Phys. Rev. B* **1991**, *44*, 9739.

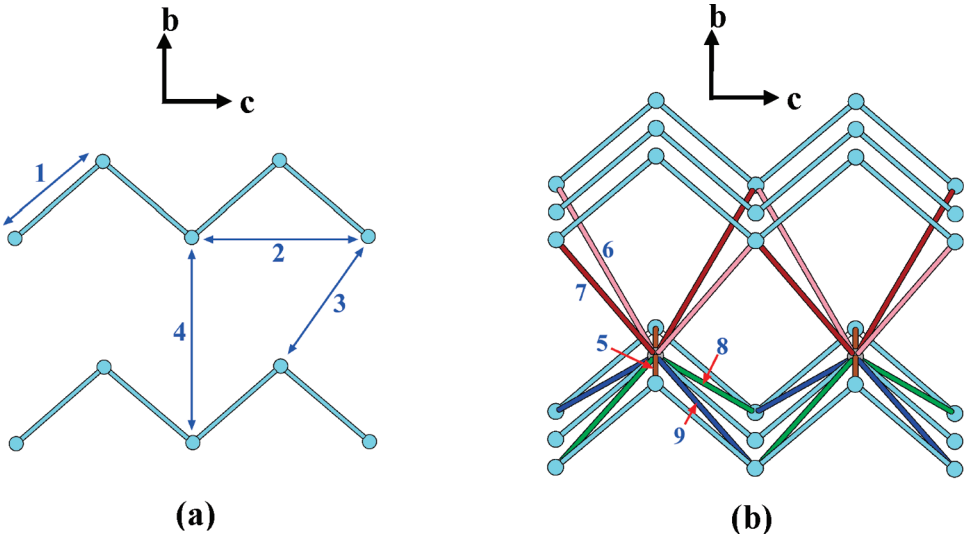

Figure 17. (a) Four spin-exchange paths (J_1-J_4) in $MnWO_4$ within each layer of Mn^{2+} ions parallel to the *bc*-plane. (b) Five spin-exchange paths (J_5-J_9) between adjacent //*bc*-layers of Mn^{2+} ions in $MnWO_4$. The numbers 1−9 refer to the spin exchange paths J_1-J_9, respectively.

critical temperature, if this transition is driven by magnetic order and is associated with the onset of the AF2 order, as in $MnWO_4$.

As in $MnWO_4$, the low-temperature magnetic ordering in the doped systems should arise from competing magnetic interactions in the presence of weak magnetic anisotropy at each Mn^{2+} site.[12,15] The outcome of this competition is likely to be modified because of the suppression of magnetic couplings by the site dilution. Nevertheless, our findings show that the multiferroic state is supported even for a doping concentration as high as $x = 0.3$. Indeed, the absence of dielectric dispersion and the sharpness of the ferroelectric peak, even for the most-substituted samples, support a long-range ferroelectric order, which is associated with a AF2-like spin-spiral magnetic structure. Assuming a random distribution of the nonmagnetic M^{2+} ions in $Mn_{1-x}M_xWO_4$, the corresponding distribution of MnO_4 chain segments along the *c*-axis is characterized by an average segment length of $L \approx 1/x$. This means that the multiferroic state exists even when short segments are created by the dilution. In addition, this implies that the nearest-neighbor intrachain spin-exchange interaction is not crucial in stabilizing the multiferroic state. The next-nearest-neighbor intrachain and interchain couplings should be important for the multiferroicity of $Mn_{1-x}M_xWO_4$.

Therefore, it is of interest to discuss the aforementioned observation from the viewpoint of the spin-exchange paths and their values in $MnWO_4$. The magnetic properties of $MnWO_4$ have been described by nine spin exchange parameters,[15,27] i.e., four exchange interactions (J_1-J_4) within each layer of Mn^{2+} ions parallel to the *bc*-plane (hereafter, the //*bc*-layer of Mn^{2+} ions) and five exchange interactions (J_5-J_9) between adjacent //*bc*-layers of Mn^{2+} ions (Figure 17). Ehrenberg et al.[27] interpreted the results of their inelastic neutron scattering measurements for $MnWO_4$, in terms of these nine spin exchange parameters. In their study, J_1 is antiferromagnetic (AFM) while J_2 is ferromagnetic (FM), so that the spin exchanges within a zigzag chain of Mn^{2+} ions parallel to the *c*-direction (hereafter, the //*c*-chain of Mn^{2+} ions) are not spin-frustrated. This is not consistent with the experimental observation that each //*c*-chain of Mn^{2+} ions exhibits a spiral spin order in the AF2 state, because the noncollinear spin order requires the presence of substantial spin frustration.[28,29] In the AF2 state, a spiral spin order occurs along the *a*-direction as well, implying that the spin-exchange interactions between //*c*-chains of Mn^{2+} ions along the *a*-direction are also spin-frustrated. The spin-exchange parameters extracted on the basis of first-principles density functional theory (DFT) calculations[15] show that both J_1 and J_2 are AFM, and J_2 is stronger than J_1 in strength. This creates spin frustration within each //*c*-chain of Mn^{2+} ions. Furthermore, because J_2 is substantial, the intrachain spin frustration would not be easily destroyed by introducing a nonmagnetic dopant (e.g., Mg^{2+} or Zn^{2+}) into the zigzag chain of Mn^{2+} ions, because the two chain segments of Mn^{2+} ions separated by a diamagnetic dopant M^{2+} can still interact across the dopant via J_2. The DFT calculations also show[15] that the interactions between the //*c*-chains of Mn^{2+} ions along the *a*-direction are spin-frustrated. This also indicates that the interlayer spin frustration along the *a*-direction is not easily broken by introducing nonmagnetic dopants into the zigzag chain of Mn^{2+} ions. Thus, the persistence of spin frustration along the *c*- and *a*-directions under nonmagnetic doping explains why the AF2 state survives the Mg and Zn substitutions.

(27) Ehrenberg, H.; Weitzel, H.; Fuess, H.; Hennion, B. *J. Phys.: Condens. Matter* **1999**, *11*, 2649.

(28) (a) Xiang, H. J.; Whangbo, M.-H. *Phys. Rev. Lett.* **2007**, *99*, 257203. (b) Xiang, H. J.; Lee, C.; Whangbo, M.-H. *Phys. Rev. B: Rapid Commun.* **2007**, *76*, 220411(R). (c) Xiang, H. J.; Wei, S.-H.; Whangbo, M.-H.; Da Silva, J. L. F. *Phys. Rev. Lett.* **2008**, *101*, 037209.

(29) (a) Greedan, J. E. *J. Mater. Chem.* **2001**, *11*, 37. (b) Dai, D.; Whangbo, M.-H. *J. Chem. Phys.* **2004**, *121*, 672.

5. Concluding Remarks

Our study shows that polycrystalline samples of $Mn_{1-x}MWO_4$ (M = Mg, Zn) solid solutions can be obtained for x up to 0.3. The substitution of the nonmagnetic ions Mg^{2+} and Zn^{2+} for the magnetic ions Mn^{2+} result in very similar effects on the magnetic and dielectric properties of $MnWO_4$. These substitutions destabilize the nonpolar magnetic structure AF1 of $MnWO_4$ but do not suppress the AF3-to-AF2 magnetoelectric phase transition. This indicates that the nonmagnetic dopants destroy neither the three-dimensional nature of magnetic interactions nor the spin frustration within each //c-chain and between //c-chains along the a-direction. Simple nonmagnetic dilution effects explain the reduction of the phase-transition temperatures T_N and T_2 by Mg and Zn substitutions. Zero-field as well as field-dependent single-crystal studies are necessary to reveal much more detail on the effects of these nonmagnetic substitutions on the low-temperature magnetic and electric properties.

Acknowledgment. We thank French Centre National de la Recherche Scientifique (CNRS) for providing L.M. with a postdoctoral fellowship. The research at IMN and ICMCB was supported in part by the GDR 3163 Program of the French CNRS. M.-H.W thanks U.S. DOE for the financial support (Grant No. DE-FG02-86ER45259). M.J. and M.M. thank Dr. R. Decourt for his support concerning the dielectric measurement setup.